Strong interfacial exchange field in the graphene/EuS heterostructure

Peng Wei[1,2]*, Sunwoo Lee[3,4], Florian Lemaitre[3,5]†, Lucas Pinel[3,5]†, Davide Cutaia[3,6], Wujoon Cha[7], Ferhat Katmis[1,2], Yu Zhu[3], Donald Heiman[8], James Hone[7], Jagadeesh S. Moodera[1,2] and Ching-Tzu Chen[3]*

Exploiting 2D materials for spintronic applications can potentially realize next-generation devices featuring low power consumption and quantum operation capability[1-3]. The magnetic exchange field (MEF) induced by an adjacent magnetic insulator enables efficient control of local spin generation and spin modulation in 2D devices without compromising the delicate material structures[4,5]. Using graphene as a prototypical 2D system, we demonstrate that its coupling to the model magnetic insulator (EuS) produces a substantial MEF (>14 T) with the potential to reach hundreds of tesla, which leads to orders-of-magnitude enhancement of the spin signal originating from the Zeeman spin Hall effect. Furthermore, the new ferromagnetic ground state of Dirac electrons resulting from the strong MEF may give rise to quantized spin-polarized edge transport. The MEF effect shown in our graphene/EuS devices therefore provides a key functionality for future spin logic and memory devices based on emerging 2D materials in classical and quantum information processing.

The MEF in magnetic multilayers can potentially reach tens or even hundreds of tesla[6]. Single-atomic-layer (two-dimensional (2D)) materials, such as graphene, monolayer WS_2 and so on, are expected to experience the strongest MEF in heterostructures with magnetic insulators owing to the short-range nature of magnetic exchange coupling[4]. 2D-material/magnetic-insulator heterostructures enable local spin modulation by magnetic gates[4,5,7], and the realization of efficient spin generation for spintronic applications[8,9].

As a proof of concept, here we demonstrate substantial MEF and spin polarization in chemical vapour deposition (CVD)-graphene/EuS heterostructures. We have chosen EuS as a model magnetic insulator because of its wide bandgap (1.65 eV), large exchange coupling $J \sim 10$ meV, and large magnetic moment per Eu ion $\langle S_z \rangle \sim 7\mu_B$ (ref. 10), yielding large estimated exchange splitting $\Delta \propto J \langle S_z \rangle$ in graphene[4,5]. EuS has also been shown to spin-polarize quasiparticles in materials including superconductors and topological insulators[6,11]. The strength of the MEF depends critically on the interface and EuS quality[12,13], which we optimize with an *in situ* cleaning and synthesis process (Methods and Fig. 1a). In contrast to other means, such as defect- or adatom-induced spin polarization[14,15], depositing insulating EuS well preserves graphene's chemical bonding, confirmed by Raman spectroscopy (Fig. 1b).

The slight enhancement of the Raman D-peak suggests that EuS deposition introduces a small number of scattering centres, as reflected in the decrease in electronic mobility (see Supplementary Information 1.) However, most graphene/EuS devices develop Shubnikov–de Haas oscillations in field ≥2 T at 4.2 K, and the lowest quantum Hall plateaus locate exactly at $2e^2/h$ (Supplementary Fig. 5-1), indicative of high graphene quality and well-preserved Dirac band structure.
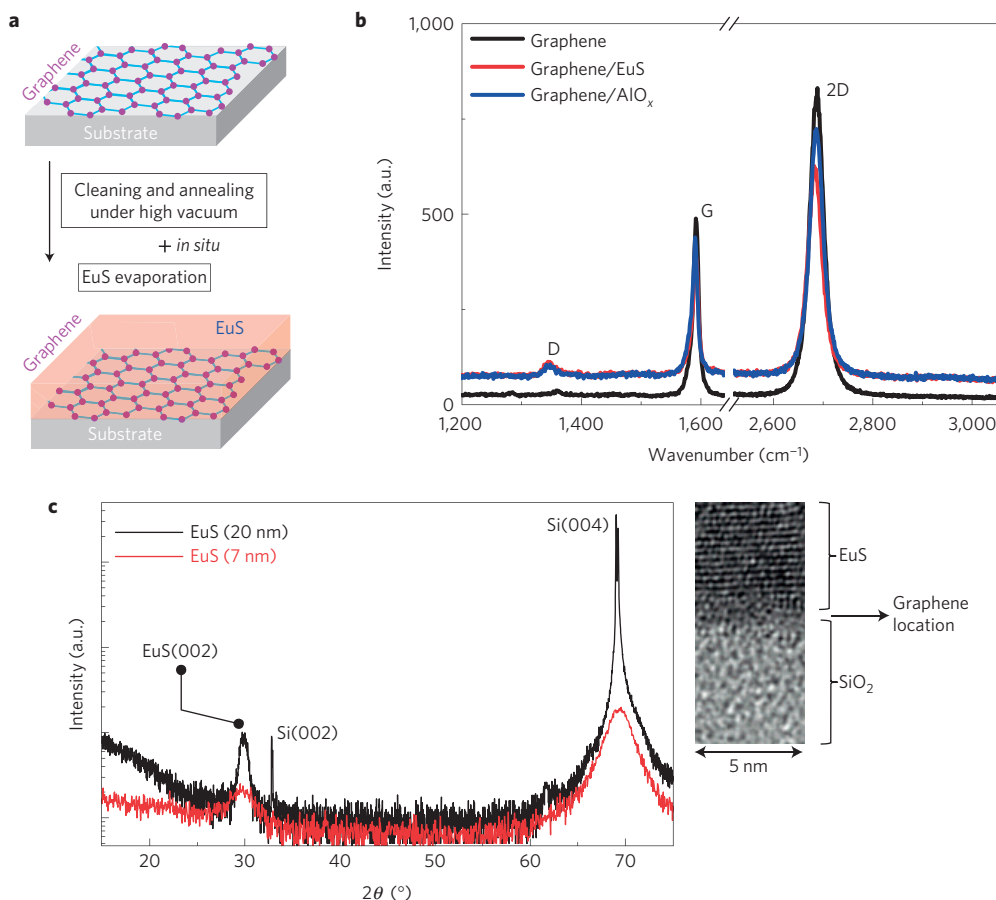
We use the Zeeman spin Hall effect (ZSHE) to probe the MEF in graphene that splits the Dirac cone through the Zeeman effect and generates electron- and hole-like carriers with opposite spins near the Dirac point V_D (Fig. 2a right panel)[8,9]. Under a Lorentz force, these electrons and holes propagate in opposite directions, giving rise to a pure spin current and non-local voltage V_{nl} (Fig. 2a left panel). We measure the non-local resistance R_{nl} of the ZSHE using the device configuration in Fig. 2a (see Methods). Figure 2b plots R_{nl} as a function of the back-gate voltage V_g under a series of applied field $\mu_0 H$ for a graphene/EuS device. The R_{nl} peak at $V_g = V_D$ can be described by[8,9,16,17]:

$$R_{nl,D} \propto \frac{1}{\rho_{xx}} \left(E_Z \frac{\partial \rho_{xy}}{\partial \mu} \right)^2 \Bigg|_{\mu_D} \qquad (1)$$

where ρ_{xx} (ρ_{xy}) is the longitudinal (Hall) resistivity, E_Z is the Zeeman splitting energy, and μ is the chemical potential. As shown in Fig. 2c, $R_{nl,D}$ in graphene/EuS easily dwarfs that in pristine graphene by a factor of ~ 8, revealing a substantial E_Z enhancement. Moreover, after prolonged air exposure (~ 1 month), $R_{nl,D}$ decreases significantly owing to degraded EuS magnetic properties by oxidation.

We further confirm the effect of EuS using correlated studies of transport and magnetization. Figure 2d shows that both $R_{nl,D}$ and magnetization M in graphene/EuS rise abruptly as T drops below T_C (~ 16 K) of EuS. On the other hand, the weak T dependence of $R_{nl,D}$ in graphene/AlO_x (Fig. 2d inset) is consistent with that in graphene/EuS above T_C. The $R_{nl,D}$ at $T > T_C$ reflects the contributions from the applied-field-induced ZSHE[7,9], and the paramagnetic response of EuS at high field (for example, 3.5 T)[10,11]. Nevertheless, the MEF-induced $R_{nl,D}$ dominates in graphene/EuS when $T < T_C$. Last, Fig. 2e demonstrates that in comparison with the longitudinal resistance R_{xx}, R_{nl} shows a tenfold larger change in

711

Figure 1 | Synthesis and characterization of graphene/EuS heterostructures. a, Process for *in situ* cleaning and deposition of graphene/EuS heterostructures under high vacuum (see Methods). **b**, Comparison between the Raman spectroscopy data of pristine graphene (black line), graphene/EuS (red line) and graphene/AlO$_x$ (blue line). Both EuS and AlO$_x$ deposition preserve graphene's lattice structure. The characteristic graphene peaks G and 2D with respect to the baseline show negligible changes. The defect D peak shows a slight increase in the spectral weight. **c**, Left panel: the wide-angle X-ray diffraction studies on our graphene/EuS heterostructure films with different EuS thickness (7 nm and 20 nm). Both EuS films show the same crystalline orientation with a (002) diffraction peak, which confirms the high-quality, single-phase film growth. Right panel: a transmission electron microscopy cross-sectional image of a typical graphene/EuS(7 nm) heterostructure showing a sharp interface.

magnitude and a much narrower peak under finite field, thereby excluding the Ohmic contribution. In contrast, the small zero-field R_{nl} does scale with R_{xx}, providing a quantitative estimate of the Ohmic contribution (see Supplementary Information 2.1). Other extrinsic effects are further discussed and ruled out (see Supplementary Information 2).

To estimate the E_Z enhanced by the MEF, we compare the field dependence of $R_{nl,D}$ in graphene/EuS with that in graphene/AlO$_x$ (Fig. 3a) fabricated from the same batch of CVD graphene. The normalized $R_{nl,D}(\mu_0 H)/R_{nl,D}(3.8\,\text{T})$ variation in graphene/EuS is almost two orders of magnitude larger, indicative of a strong contribution from EuS. $R_{nl,D}(3.8\,\text{T})$ is chosen as the reference because ZSHE dominates the non-local signal at large field.

According to equation (1) and previous reports[9,16,17], $R_{nl,D}$ can be recast as

$$R_{nl,D} = R_0 + \beta\,(\mu_0 H) \cdot E_Z^2 \qquad (2)$$

Here R_0 accounts for the zero-field non-local signal from extrinsic sources (see Supplementary Information 2), the parameter β represents the orbital-field effect manifested by ρ_{xx} and ρ_{xy}, and $E_Z = g\mu_B B_Z = g\mu_B (B_{exc} + \mu_0 H)$, where B_{exc} is the MEF. We further define the parameter α:

$$\alpha^2(\mu_0 H) \equiv \frac{\beta\,(\mu_0 H)}{\beta\,(\mu_0 H_0)} = \left(\frac{E_{Z0}}{E_Z}\right)^2 \cdot \left[\frac{R_{nl,D}(\mu_0 H) - R_0}{R_{nl,D}(\mu_0 H_0) - R_0}\right] \qquad (3)$$

where E_{Z0} denotes the Zeeman energy at the reference field $\mu_0 H_0$. Given H_0, deriving $\alpha(\mu_0 H)$ of graphene/AlO$_x$ is straightforward because E_Z is solely determined by $\mu_0 H$. The inset of Fig. 3b shows the calculated α using $\mu_0 H_0 = 1\,\text{T}$, a proper reference field as we will explain below.

To derive α of graphene/EuS, we note that according to the theory of the ZSHE[9,17], α depends on sample mobility. Other sample-dependent terms (including spin relaxation length, density of thermally activated carriers and Fermi velocity) cancel out (see Supplementary Information 3). The mobility difference between our graphene/EuS and graphene/AlO$_x$ samples is ~25% (see Supplementary Information 1), which would yield only a ~10% correction to α (see Supplementary Information 3). As ~10% difference is small, for an order-of-magnitude estimate of the MEF, we adopt the α value of graphene/AlO$_x$ for graphene/EuS as an approximation. We then evaluate E_Z in graphene/EuS using

$$E_Z = \frac{E_{Z0}}{\alpha} \sqrt{\frac{R_{nl,D}(\mu_0 H) - R_0}{R_{nl,D}(\mu_0 H_0) - R_0}}$$

To obtain the lower bound of E_Z, we approximate $E_{Z0} \approx g\mu_B\mu_0 H_0$, ignoring the B_{exc} contribution. This constrains us to use a small H_0 such that B_{exc} is small. Meanwhile, H_0 should be high enough to ensure that $R_{nl,D}(\mu_0 H_0) - R_0$ is much larger than noise. Therefore,
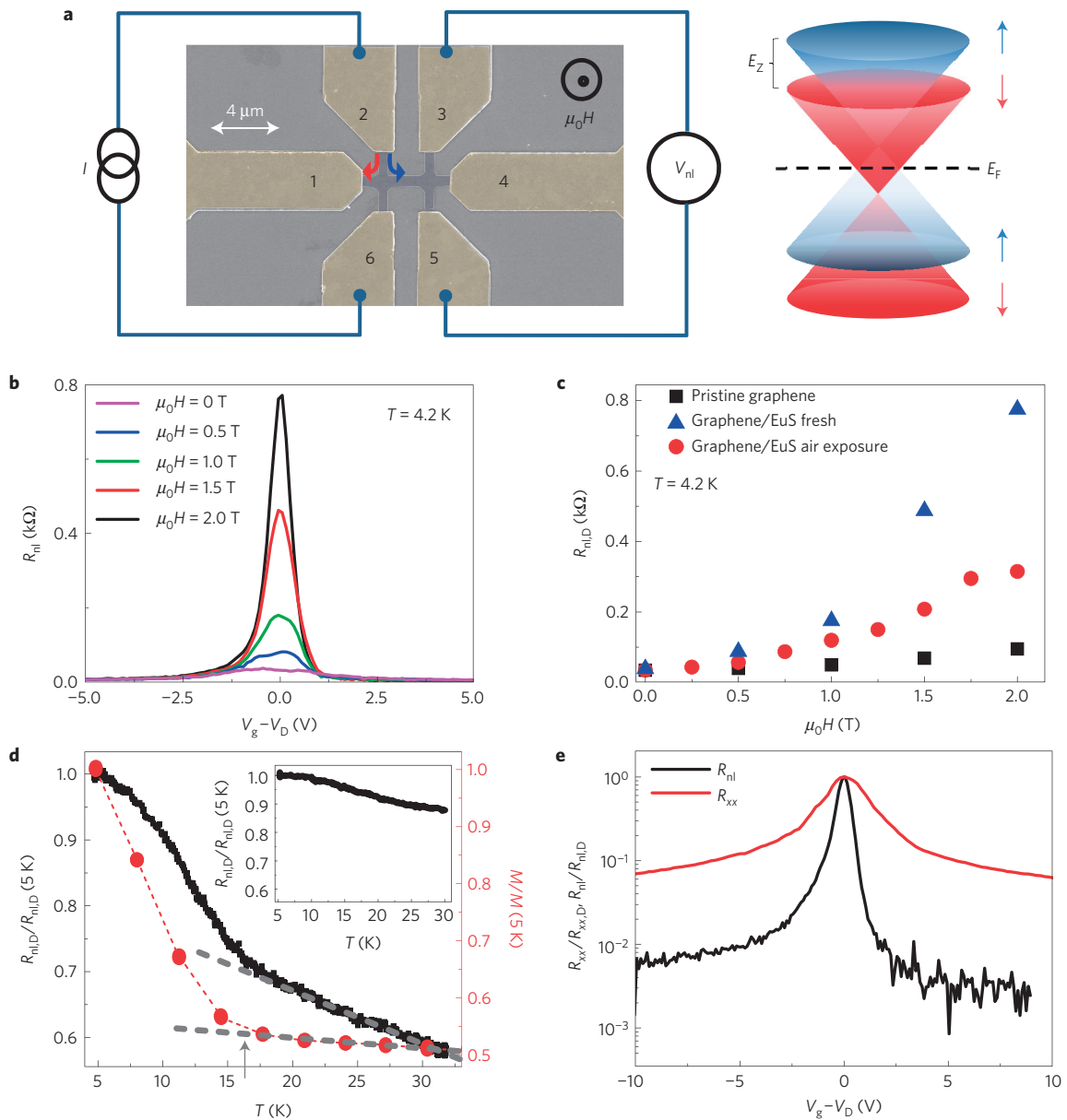
Figure 2 | Zeeman spin Hall effect in graphene/EuS heterostructures. a, Left panel: a false-coloured device image taken by a scanning electron microscope. The central Hall bar region is graphene coated with EuS. The outer regions (1–6) are Ti/Pd/Au electrodes. Typical non-local measurements are carried out by applying current I along leads 2 and 6 and measuring non-local voltage V_{nl} between leads 3 and 5. The non-local resistance is defined as $R_{nl} \equiv (V_{nl}/I)$. Right panel: a schematic drawing of the Zeeman splitting of the Dirac cone in graphene and the spin-up hole-like and spin-down electron-like carriers at the charge neutrality point. The applied field $\mu_0 H$ directs the oppositely spin-polarized charge carriers towards opposite directions along the Hall bar channel, generating a pure transverse spin current and namely the ZSHE. A non-local voltage drop is developed across the other pair of electrodes through the inverse effect. The black dashed line indicates the Fermi level (E_F) when it coincides with the charge neutrality point where the non-local voltage is largest. The flow of the spin-up (spin-down) current is shown by the blue (red) arrows in the scanning electron micrograph. **b**, Non-local resistance R_{nl} as a function of gate voltage V_g under different $\mu_0 H$ for a CVD-graphene/EuS device at temperature T. At finite field, the large R_{nl} peak near the bias voltage corresponding to the Dirac point (V_D) is the signature of the ZSHE. At zero field, the R_{nl} peak is very small, demonstrating negligible Ohmic contribution. **c**, Comparison of $R_{nl,D}$ (the R_{nl} value at the Dirac point V_D) versus $\mu_0 H$ curves for the graphene device before (pristine) and after EuS deposition. Also plotted is the same graphene/EuS device after prolonged air exposure (∼1 month), which shows that $R_{nl,D}$ strongly depends on the EuS quality. We note that the carrier mobility in graphene hardly varies after the air exposure (see Supplementary Information 1). **d**, Comparison of the temperature dependence of $R_{nl,D}$ (black line) and of M (red circles, measured by a superconducting quantum interference device) of the graphene/EuS heterostructure, confirming the magnetic origin of R_{nl}. Both data traces show an onset at ∼16 K (indicated by the grey arrow) where EuS undergoes the ferromagnetic–paramagnetic transition. The $R_{nl,D}$ data set is taken at $\mu_0 H = 3.5$ T. The red dashed line is the spline line to the magnetization data. The grey dashed lines indicate the temperature-dependence data above the EuS transition temperature T_C. The symbols represent actual data and the dashed lines are guides to the eyes. Inset: the temperature dependence of $R_{nl,D}$ of graphene/AlO$_x$ at $\mu_0 H = 3.5$ T. The change in $R_{nl,D}$ is much weaker with no discernible onset feature. The gradual variation in $R_{nl,D}$ is consistent with the high-temperature background ($T > T_C$) of the graphene/EuS curve in the main panel. **e**, Comparison of the normalized non-local resistance ($R_{nl}/R_{nl,D}$) and longitudinal resistance ($R_{xx}/R_{xx,D}$) at $\mu_0 H = 2.0$ T in graphene/EuS. $R_{nl,D}$ and $R_{xx,D}$ denote the resistance values at the Dirac point. The change in $R_{nl}/R_{nl,D}$ is one order of magnitude larger than $R_{xx}/R_{xx,D}$, thereby ruling out the Ohmic contribution as a primary source of the measured R_{nl} under finite field.
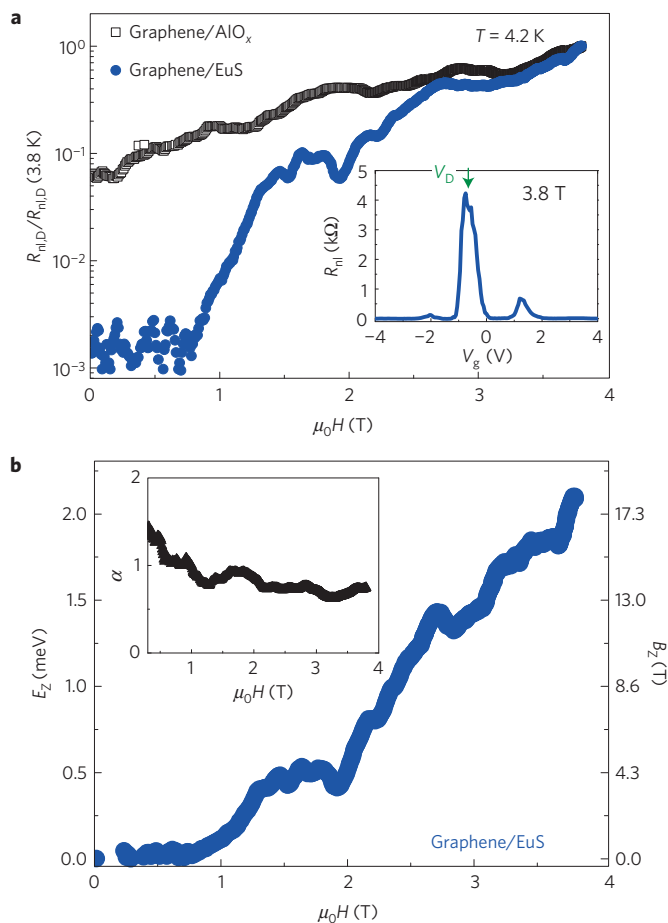
Figure 3 | Estimate of the graphene/EuS interfacial exchange field using Zeeman spin Hall signals. a, Field dependence of $R_{nl,D}$ in graphene/EuS versus that in graphene/AlO$_x$, plotted in the form of normalized $R_{nl,D}/R_{nl,D}(3.8\,T)$. It shows orders-of-magnitude difference in the field-induced enhancement. The non-local resistance in graphene/AlO$_x$ (black squares) increases gradually with the applied field. In contrast, the non-local resistance in graphene/EuS (blue circles) rises sharply at ~0.9 T. This onset behaviour is commonly observed in graphene/EuS samples; however, it is absent in pristine graphene or graphene/AlO$_x$ (for example, Figs 2c and 3a). We infer from the value of the estimated Zeeman splitting (E_Z) in Fig. 3b that the onset behaviour develops when E_Z is close to overcoming the thermal energy $k_B T$ (~0.36 meV at 4.2 K), above which thermal smearing may no longer reduce the ZSHE. Inset: R_{nl} versus V_g data of graphene/EuS at $\mu_0 H = 3.8\,T$, showing LL quantization and a pronounced EuS-induced ZSHE peak indicated by the green arrow. **b**, Quantitative estimation of the Zeeman splitting energy E_Z in the presence of EuS. The curve represents the lower-bound estimate as elucidated in the main text. On top of the main curve, several secondary structures are seen. As these features are history dependent (irreversible on thermal cycling and field cycling) we infer that these secondary features may be attributed to the multi-domain magnetization process of EuS, during which the spin current generation and transport may be modified by magnetic domains or domain walls. The right axis shows the estimated total Zeeman field (B_Z) in graphene enhanced by the EuS-induced interfacial exchange field. Inset: field dependence of the dimensionless coefficient $\alpha \equiv \sqrt{(\beta(\mu_0 H))/(\beta(\mu_0 H = 1\,T))}$ that captures the orbital-field effect in non-local resistance. α is extracted from the graphene/AlO$_x$ data in **a** where the interface exchange field is zero and the total Zeeman field equals the applied field.

we choose $H_0 \approx 1\,T$, above and close to the onset of $R_{nl,D}$ (Fig. 3a). The calculated lower-bound estimate of E_Z is plotted against

the applied field in Fig. 3b. We further take the free-electron gyromagnetic factor $g = 2$ to estimate B_Z and find that it reaches a significant value of $> 18\,T$ when $\mu_0 H \sim 3.8\,T$ (Fig. 3b). Moreover, the spin generation efficiency of ZSHE characterized by the spin Hall angle θ_{SH} is enhanced from $\theta_{SH} \sim (0.51 \pm 0.10)$ at $\mu_0 H = 2\,T$ in pristine graphene to $\theta_{SH} \geq 1.22$ in graphene/EuS—more than a factor of 2 gain. In contrast to conventional spin injection in which spin-polarized electrons tunnel into 2D materials through a barrier[18], the MEF directly polarizes the 2D electrons, thereby circumventing issues of pinholes and barrier breakdown.

The intense MEF also lifts the ground-state degeneracy of graphene in the quantum Hall regime. In graphene/EuS, the quantum Hall regime is reached at $\mu_0 H \simeq 3.8\,T$ (Fig. 4a). The filling factor ν of the Landau level (LL) obeys: $\nu = \pm 4(|n| + 1/2)$ for 2D Dirac fermions where $n = 0, 1, 2\ldots$ is the LL index. ν can be derived from the gate voltage at each R_{xx} minimum (Fig. 4a inset). By tracing the $\nu = \pm 2$ fillings with $\mu_0 H$, we find that the corresponding electron density depends only on $\mu_0 H$ but not on B_Z (Fig. 4b and Supplementary Figs 2–5), implying that EuS causes negligible orbital field. Nevertheless, a close look at the R_{xx} maxima reveals extra dip features that develop with increasing $\mu_0 H$, especially at the $n = 0$ LL (Fig. 4c). This peak-splitting feature indicates the lifting of LL degeneracy under large B_Z, which can be well fitted by simple Gaussians (Fig. 4d). The observed splitting feature is reproducible in both R_{xx} and R_{nl} (inset of Fig. 4d) and the associated plateau feature is also observable in the R_{xy} measurements (see Supplementary Information 5).

Another observation associated with the intense B_Z is the reduction of $R_{xx,D}$, longitudinal resistance at the Dirac point. As shown in Fig. 4e, $R_{xx,D}$ initially increases with $\mu_0 H$ until it peaks at ~2 T and then drops continuously with field. At 3.8 T, $R_{xx,D}$ is even smaller than its zero-field value, in sharp contrast to the monotonic increase of $R_{xx,D}$ in graphene/AlO$_x$ (Fig. 4e inset) and in previous reports[19–21]. The divergent $R_{xx,D}$ is usually attributed to the gapped $\nu = 0$ state under a perpendicular field[22,23]. The $\nu = 0$ state originates from the splitting of $n = 0$ LL and can either be a valley-polarized spin singlet (Fig. 4f) or a spin-polarized valley singlet (Fig. 4g) depending on the relative strength of valley versus spin splitting[22–24]. As the valley-polarized state inevitably leads to divergent $R_{xx,D}$, the observed decrease of $R_{xx,D}$ in graphene/EuS strongly suggests the spin-polarized valley-singlet state. That $R_{xx,D}(3.8\,T) < R_{xx,D}(0\,T)$ further indicates additional states forming at the Dirac point with increasing B_Z, consistent with the presence of counter-propagating edge channels in the spin-polarized $\nu = 0$ state (Fig. 4g) similar to the quantum spin Hall effect (Fig. 4g inset)[22,25,26]. Such an unusual ground state had only been created under an enormous in-plane field ($\mu_0 H > 20\,T$) in selected high-quality graphene devices[22,25]. Here we show that it is accessible in a much lower field using scalable CVD graphene by leveraging the MEF. Thus, our approach enables other emerging phenomena, for example the quantum anomalous Hall effect in 2D materials by engineering magnetic insulators with inherently both MEF and spin–orbit-coupling[27,28], or magnetically gated information storage/processing devices with strong spin–orbit-coupling in 2D transition metal dichalcogenides using MEF[3,29]. For industrial applications in low-power information processing, development of high-quality magnetic insulators that are compatible with 2D materials and magnetic above room temperature will be highly desirable.

Methods

Methods and any associated references are available in the online version of the paper.
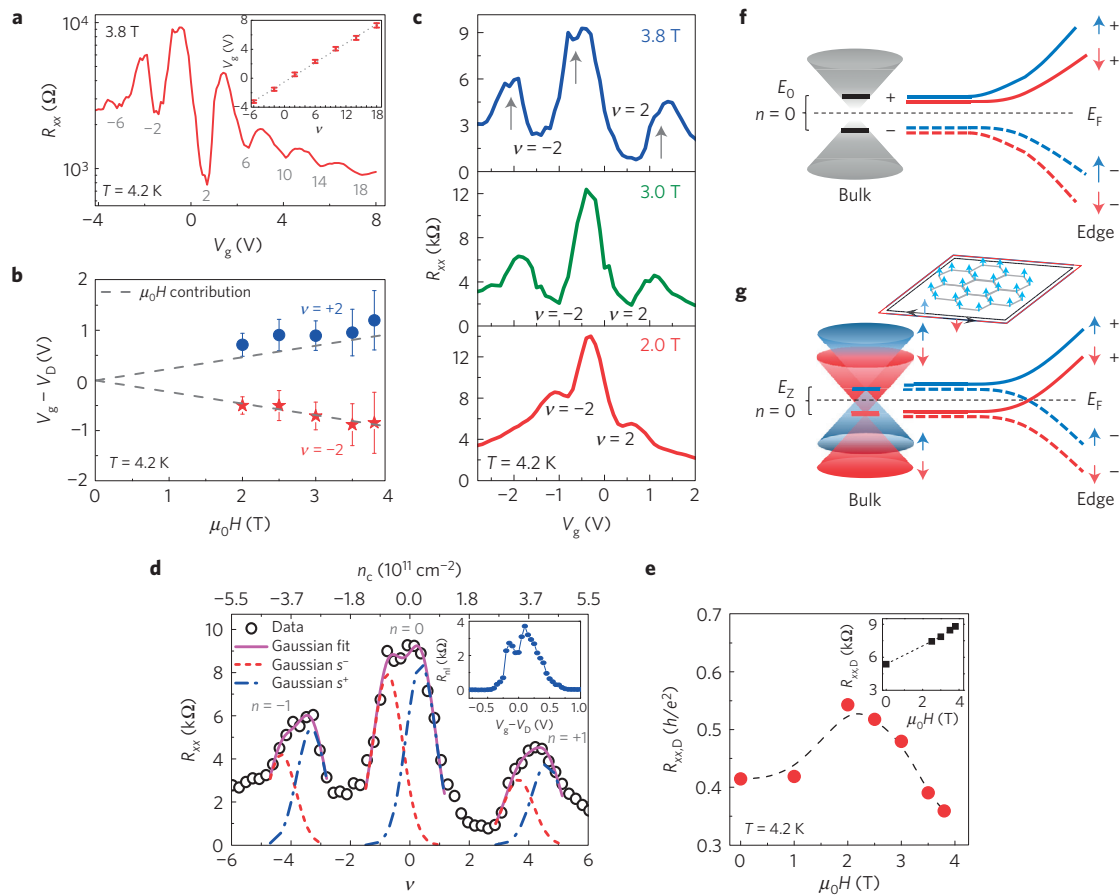
Figure 4 | Effect of strong interfacial exchange field in the quantum Hall regime. a, Magnetoresistance (R_{xx}) as a function of the gate voltage V_g of the graphene/EuS device in Fig. 3, showing pronounced quantum oscillations at $\mu_0 H = 3.8\,T$. The LL filling factors ν corresponding to each R_{xx} minimum are labelled in light grey. Inset: V_g corresponding to each ν. The error bars in the inset are determined by the uncertainty in the bias voltage reading for each LL filling (local minima of R_{xx}). The dotted line is the linear fit to the data. From the intercept at $\nu = 0$, we determine the Dirac point V_D. **b**, Field dependence of the gate voltage ($V_g - V_D$) at $\nu = \pm 2$ extracted from the magnetoresistance curves. The error bars are determined by the uncertainty in the bias voltage reading for $\nu = \pm 2$ fillings (local minima of R_{xx}). The dashed lines plot the calculated voltage values, taking into account only the applied field $\mu_0 H$ contribution. The predicted V_g matches well with the experimental data (symbols) within the error bar, which proves that the orbital effect induced by EuS is negligible. **c**, R_{xx} versus V_g data of graphene/EuS under different applied fields: 2.0 T, 3.0 T and 3.8 T. Quantum oscillations in R_{xx} are observable down to $\mu_0 H = 2.0\,T$. In contrast to the single peaks at 2 T, the main peak of R_{xx} near the Dirac point develops double-peak features at 3.8 T denoted by the grey arrows, which suggests the splitting of the LL. Notably, the height of the R_{xx} peak at the Dirac point decreases as $\mu_0 H$ increases. **d**, Gaussian fit of the R_{xx} versus V_g data at 3.8 T in **c** to quantify the LL splitting. The x axis has been converted to ν according to the fitted values of V_D and $(d\nu/dV_g)$ in **a**. The corresponding carrier density n_c in graphene is given on the upper x axis. The splitting of the $n = \pm 1$ and $n = 0$ LLs is located at $\nu = \pm 4$ and $\nu = 0$ respectively, which indicates half-filling of the $n = \pm 1$ and $n = 0$ LLs due to spin splitting. Here n represents the LL index. Simple Gaussians centred at each sub-peak (sub-LL): $R_{xx}^{peak} \propto (1/\gamma\sqrt{2\pi})e^{-(V_g - V_0)^2/2\gamma^2}$ are used to identify the splitting. Here γ describes the impurity broadening, and V_0 specifies the centre of the split sub-peak. Each $n = 0$ and ± 1 LLs is fitted by the superposition of two Gaussians with the same γ. The solid line shows the fitting curve with a coefficient of determination ~ 0.96; the dash-dotted and dashed lines show the individual Gaussian components for each sub-peaks denoted as s^+ and s^-, respectively. Inset: the splitting of the $n = 0$ LL is also observed in the non-local resistance R_{nl} (see Supplementary Fig. 5-1(a).) **e**, The resistance peak at the Dirac point $R_{xx,D}$ as a function of $\mu_0 H$. Symbols represent the actual data, and the dashed line is a guide to the eyes. $R_{xx,D}$ increases with $\mu_0 H$ at small field but decreases significantly above 2 T, in contrast to the diverging $R_{xx,D}$ in the valley-polarized spin-singlet $\nu = 0$ state shown in **f**. Inset: monotonic increase of $R_{xx,D}$ versus $\mu_0 H$ in the control sample graphene/AlO$_x$. **f**, Schematic of the valley-polarized spin-singlet $\nu = 0$ state in which the bulk gap at the Dirac cone is dominated by the valley splitting E_0. The arrows indicate the spins. The '+' and '−' indicate different valleys. The resistance R_{xx} diverges as the chemical potential is scanned across the charge neutrality point within the gap. **g**, Schematic of the spin-polarized valley-singlet $\nu = 0$ state in which the bulk gap at the Dirac cone is dominated by the Zeeman splitting E_Z. The sub-LLs of the spin-up cone and spin-down cone crossover in energy near the edge of the sample, leading to counter-propagating edge channels with opposite spins (see inset). The presence of the edge channels agrees with the observation of decreasing $R_{xx,D}$ and $R_{xx,D}$ (3.8 T) $< R_{xx,D}$ (0 T) in **e**. Inset: schematic illustration of the vertically aligned spins in graphene by the EuS exchange field, leading to a ferromagnetic ground state.

References

1. Tombros, N., Jozsa, C., Popinciuc, M., Jonkman, H. T. & van Wees, B. J. Electronic spin transport and spin precession in single graphene layers at room temperature. *Nature* **448,** U571–U574 (2007).
2. Han, W., Kawakami, R. K., Gmitra, M. & Fabian, J. Graphene spintronics. *Nature Nanotech.* **9,** 794–807 (2014).
3. Xu, X., Yao, W., Xiao, D. & Heinz, T. F. Spin and pseudospins in layered transition metal dichalcogenides. *Nature Phys.* **10,** 343–350 (2014).
4. Haugen, H., Huertas-Hernando, D. & Brataas, A. Spin transport in proximity-induced ferromagnetic graphene. *Phys. Rev. B* **77,** 115406 (2008).
5. Yang, H. X. *et al*. Proximity effects induced in graphene by magnetic insulators: first-principles calculations on spin filtering and exchange-splitting gaps. *Phys. Rev. Lett.* **110,** 046603 (2013).
6. Li, B. *et al*. Superconducting spin switch with infinite magnetoresistance induced by an internal exchange field. *Phys. Rev. Lett.* **110,** 097001 (2013).

7. Semenov, Y. G. Spin field effect transistor with a graphene channel. *Appl. Phys. Lett.* **91,** 153105 (2007).
8. Abanin, D. A. *et al.* Giant nonlocality near the Dirac point in graphene. *Science* **332,** 328–330 (2011).
9. Abanin, D. A., Gorbachev, R. V., Novoselov, K. S., Geim, A. K. & Levitov, L. S. Giant spin-Hall effect induced by the Zeeman interaction in graphene. *Phys. Rev. Lett.* **107,** 096601 (2011).
10. Moodera, J. S., Santos, T. S. & Nagahama, T. The phenomena of spin-filter tunnelling. *J. Phys. Condens. Matter* **19,** 165202 (2007).
11. Wei, P. *et al.* Exchange-coupling-induced symmetry breaking in topological insulators. *Phys. Rev. Lett.* **110,** 186807 (2013).
12. Swartz, A. G., Odenthal, P. M., Hao, Y., Ruoff, R. S. & Kawakami, R. K. Integration of the ferromagnetic insulator EuO onto graphene. *ACS Nano* **6,** 10063–10069 (2012).
13. Swartz, A. G. *et al.* Integrating MBE materials with graphene to induce novel spin-based phenomena. *J. Vac. Sci. Technol. B* **31,** 04D105 (2013).
14. Nair, R. R. *et al.* Spin-half paramagnetism in graphene induced by point defects. *Nature Phys.* **8,** 199–202 (2012).
15. McCreary, K. M., Swartz, A. G., Han, W., Fabian, J. & Kawakami, R. K. Magnetic moment formation in graphene detected by scattering of pure spin currents. *Phys. Rev. Lett.* **109,** 186604 (2012).
16. Renard, J., Studer, M. & Folk, J. A. Origins of nonlocality near the neutrality point in graphene. *Phys. Rev. Lett.* **112,** 116601 (2014).
17. Abanin, D. A., Shytov, A. V., Levitov, L. S. & Halperin, B. I. Nonlocal charge transport mediated by spin diffusion in the spin Hall effect regime. *Phys. Rev. B* **79,** 035304 (2009).
18. Han, W. *et al.* Tunneling spin injection into single layer graphene. *Phys. Rev. Lett.* **105,** 167202 (2010).
19. Zhang, Y. *et al.* Landau-level splitting in graphene in high magnetic fields. *Phys. Rev. Lett.* **96,** 136806 (2006).
20. Checkelsky, J. G., Li, L. & Ong, N. P. Zero-energy state in graphene in a high magnetic field. *Phys. Rev. Lett.* **100,** 206801 (2008).
21. Amet, F., Williams, J. R., Watanabe, K., Taniguchi, T. & Goldhaber-Gordon, D. Insulating behavior at the neutrality point in single-layer graphene. *Phys. Rev. Lett.* **110,** 216601 (2013).
22. Young, A. F. *et al.* Spin and valley quantum Hall ferromagnetism in graphene. *Nature Phys.* **8,** 550–556 (2012).
23. Alicea, J. & Fisher, M. P. A. Graphene integer quantum Hall effect in the ferromagnetic and paramagnetic regimes. *Phys. Rev. B* **74,** 075422 (2006).
24. Nomura, K. & MacDonald, A. H. Quantum Hall ferromagnetism in graphene. *Phys. Rev. Lett.* **96,** 256602 (2006).
25. Young, A. F. *et al.* Tunable symmetry breaking and helical edge transport in a graphene quantum spin Hall state. *Nature* **505,** 528–532 (2014).
26. Roth, A. *et al.* Nonlocal transport in the quantum spin Hall state. *Science* **325,** 294–297 (2009).
27. Wang, Z., Tang, C., Sachs, R., Barlas, Y. & Shi, J. Proximity-induced ferromagnetism in graphene revealed by the anomalous Hall effect. *Phys. Rev. Lett.* **114,** 016603 (2015).
28. Qiao, Z. *et al.* Quantum anomalous Hall effect in graphene from Rashba and exchange effects. *Phys. Rev. B* **82,** 161414 (2010).
29. Manchon, A., Koo, H. C., Nitta, J., Frolov, S. M. & Duine, R. A. New perspectives for Rashba spin-orbit coupling. *Nature Mater.* **14,** 871–882 (2015).

Additional information

Supplementary information is available in the online version of the paper. Reprints and permissions information is available online at www.nature.com/reprints. Correspondence and requests for materials should be addressed to P.W. or C.-T.C.

Competing financial interests

The authors declare no competing financial interests.

Methods

Wafer-size (>1 cm × 1 cm) monolayer graphene was grown on copper foils by standard chemical vapour deposition[30] (CVD). We transferred the CVD graphene samples to low-resistivity silicon substrates (<0.005 Ω cm) capped with ~100 nm custom-grown thermal oxide (gate dielectric for chemical potential tuning) and pre-patterned with gold alignment marks. We have employed two transfer techniques—the PMMA/PDMS stamping method and the recyclable pressure sensitive adhesive films method[30]. The latter is found to yield higher quality devices. The transferred graphene was first shaped into a Hall bar geometry using electron-beam lithography (Nano Beam nB4) and oxygen plasma etching (Plasma Etch PE-50). The channel width of the devices ranges from 0.5 to 1 μm, and the channel length (l) to width (w) ratio is fixed to $l/w = 2$, 2.5 and 3. Then the electrodes of Ti/Pd/Au were deposited by electron-beam evaporation. Last, to remove polymeric residues from the aforementioned fabrication processes, we have annealed the samples in high vacuum (<1×10^{-6} torr) at 170–200 °C for ~3 h to remove the organic residues from the electron-beam resist after the device fabrication. The typical field-effect mobility of the resulting devices is about 6,000 cm² V⁻¹ s. Before forming the EuS/graphene heterostructure, the Hall bar devices were annealed *in situ* at low 10^{-8} torr vacuum to remove possible water molecules on graphene and any remaining organic residues immediately before the EuS deposition. Then EuS (3 ~ 7 nm) was deposited at room temperature under 10^{-8} torr vacuum and capped with AlO_x (15 nm) to prevent oxidation. For simplicity, in the main text, we omit this capping layer when labelling the devices. Both EuS and AlO_x are grown from single-compound sources. The growth of EuS is shown to preserve the graphene layer underneath by Raman spectroscopy (Fig. 1b), and the growth of AlO_x is proved to preserve the EuS layer below[11]. The detailed characterizations of the heterostructure material are described in Supplementary Information 1. EuS grown on graphene is confirmed to have a single-phase (00L) type orientation by the clear (002) peak in X-ray diffraction data (Fig. 1c). Unlike EuO that requires an O_2 atmosphere, the growth of EuS avoids O_2 absorption on graphene and thus sidesteps the associated degradation effects. The EuS films have been proved insulating (see Supplementary Information 1.3) and do not contribute to non-local signal in the graphene/EuS heterostructure (see Supplementary Information 2.5). Unless otherwise specified, all reported data were measured at 4.2 K using the a.c. lock-in method with an excitation current of 100 nA. The electrical and magneto-transport experiments were carried out in both the non-local and standard longitudinal/Hall configurations (Fig. 2a). In the non-local configuration, current I is applied along leads 2 and 6 and voltage V_{nl} is measured between leads 3 and 5. The non-local resistance is defined as $R_{nl} \equiv (V_{nl}/I)$. In the standard transport configuration, current I is applied along 1 and 4, voltages V_{xx} is measured between either 2 and 3 or 6 and 5, and longitudinal resistance is defined as $R_{xx} \equiv (V_{xx}/I)$. Under a perpendicular field $\mu_0 H$, the Hall voltage V_{yx} is measured between either 6 and 2 or 5 and 3, and Hall resistance is defined as $R_{yx} \equiv (V_{yx}/I)$. We have measured >20 control devices on >10 different chips and ~15 surviving EuS/graphene devices on 5 different chips. (That fewer graphene/EuS chips are measured reflects the survival rate of graphene devices after EuS deposition—a result of electrostatic discharge either during deposition or in transit.) Compared with the control devices, the EuS-induced enhancement in R_{nl} response ranges from unity to ~2 orders of magnitude. We estimate that the corresponding exchange field ranges from less than 1 T to over 10 T depending on the graphene and interface quality. The magnetization measurements were performed using a standard superconducting quantum interference device magnetometer.

References

30. Kim, S. J. *et al*. Ultraclean patterned transfer of single-layer graphene by recyclable pressure sensitive adhesive films. *Nano Lett.* **15,** 3236–3240 (2015).